Chemical Engineering Journal 518 (2025) 164725

Contents lists available at ScienceDirect

Chemical Engineering Journal

journal homepage: www.elsevier.com/locate/cej

Beyond liquid density assumptions: A novel SANS-based approach to quantify adsorbed methane and adsorption-induced coal microstructure alterations

Xinxin He [a], Rui Zhang [b,*], Derek Elsworth [a], Lilin He [c], Shimin Liu [a,*]

[a] Department of Energy and Mineral Engineering, G3 Center and EMS Energy Institute, The Pennsylvania State University, University Park, PA 16802, USA
[b] Eyring Materials Center, Arizona State University, Tempe, AZ 85281, USA
[c] Neutron Scattering Division, Oak Ridge National Laboratory, Oak Ridge, TN 37831, USA

ARTICLE INFO

Keywords:
SANS
Adsorption
Methane density
Pore accessibility
Greenhouse-gas mitigation
Carbon sequestration
Microstructure alterations

ABSTRACT

This study investigates methane storage and its adsorption-induced structural changes in coal under various pressures and temperatures through small-angle neutron scattering (SANS). We introduce a direct SANS-based method to quantify micropore accessibility and demonstrate that rising external pressure not only boosts methane adsorption but also triggers detectable microstructural compaction in the organic matrix. A novel scattering model incorporating mechanical constraints is proposed to capture the interplay of micropore deformation and adsorbed methane density. Results reveal pronounced pressure amplification in nano-confined pores, up to 27-fold, yet the true adsorbed-phase density never exceeds 0.305 g/mL, substantially lower than the liquid-methane value routinely assumed. By incorporating the SANS-derived density, we accurately convert Gibbs surface excess to absolute adsorption, revealing significant underestimations ($\leq$10 % at field pressures) that arise from using liquid density approximations. Moreover, sorption-induced contractions of aromatic lamellae and the evolving micropore geometry underscore the dynamic role of microstructure in regulating gas adsorption and transport. These findings demonstrate the need to refine density corrections in sorptive gas adsorption in coal for improving assessments of coalbed methane recovery, carbon sequestration, and outburst risk. Extending the proposed methods to diverse carbonaceous media will establish a more comprehensive, pressure-dependent framework for accurate gas-storage predictions.

1. Introduction

Adsorption plays a crucial role in energy storage and carbon sequestration, particularly in natural organic rich rock like coal/shale reservoirs, where 80–90 % of methane is stored as adsorbed state within the nanoporous confined pores [1–5]. Methane transport in coal involves adsorption/desorption, diffusion and seepage, with adsorption governing storage as the source and thus influencing methane production and greenhouse gas mitigation strategies [6–11]. Those mitigation strategies extend from mine-site safety to national climate-policy compliance. In underground coal mining, inaccurate estimates of adsorbed CH_4 lead to under-predicted emissions during ventilation and post-mining desorption, whereas for CBM or carbon-capture-and-storage (CCS) projects they propagate into reserve calculations, project economics, and life-cycle greenhouse-gas balances. Adsorption capacity is primarily dictated by pore morphology and organic constituents [12–14]. Quantitatively, it is commonly characterized using Langmuir isotherms derived from adsorption experiments [15–17]. However, accurately estimating adsorption capacity remains challenging, as the volume occupied by the adsorbed gas is often neglected due to the lack of direct measurements of the adsorbed volume. Consequently, the measured adsorption corresponds to the Gibbs surface excess (GSE) [18,19], which differs from absolute adsorption, the true indicator of storage capacity. The precise estimation of gas density is crucial for determining adsorption capacity, particularly in converting GSE into absolute adsorption amounts:

$$\text{Adsorption}_{\text{absolute}} = \frac{\text{GSE}}{1 - \frac{\rho_g}{\rho_a}} \tag{1}$$

Among the correction parameters, the adsorbed methane density (ρ_a)

* Corresponding authors.
E-mail addresses: Rui.Zhang.10@asu.edu (R. Zhang), szl3@psu.edu (S. Liu).

https://doi.org/10.1016/j.cej.2025.164725
Received 8 May 2025; Received in revised form 6 June 2025; Accepted 9 June 2025
Available online 11 June 2025
1385-8947/© 2025 Elsevier B.V. All rights are reserved, including those for text and data mining, AI training, and similar technologies.

plays a critical role due to its dominant influence on adsorption in micropores. While determining the adsorbed phase density remains a topic of debate and a critical challenge. The methane adsorbed phase density has been routinely assumed to be constant at liquid methane (0.422 g/mL) [20,21]. While this assumption is sufficient for qualitative and comparative studies, its accuracy remains questionable, as experimental studies and molecular simulations demonstrate that ρ_a varies with pressure, temperature, and pore size [22–24]. For instance, molecular dynamics simulations reveal gradient methane density distributions in nanopores, with near-wall densities exceeding bulk liquid values [22,25,26]. However, discrepancies persist between idealized pore models and the complex, heterogeneous pore networks of natural coal.

Broadly, ρ_a determination encompass three complementary approaches: i) Empirical methods adopt fixed values, such as the aforementioned liquid-phase or van der Waals density (0.373 g/mL) [27,28] but fail to account for coal's structural complexity and the thermodynamic behavior of gas in real confined environments; ii) Fitting methods, including fitting and manipulation of the isotherm data, utilize modified Langmuir, Dubinin-Radushkevich (DR), or supercritical-DR (SDR) models [29–31]. However, these approaches yield widely variable results (e.g., 0.373–0.9 g/mL for identical isotherms) [32] due to model dependence and differing assumptions, which are often oversimplified or lack relevance to physical reality; iii) Direct measurements, while ideal, are rarely completed due to the complexity of the techniques involved. Measurements using nuclear magnetic resonance (NMR) spectroscopy represent a potentially promising method, as NMR detects confined CH_4 by distinguishing between adsorbed and free methane through hydrogen signal relaxation [33,34]. However, its application is limited to high pressures. Additionally, our previous multistage adsorption model [35] integrated micropore filling (0.38–1.5 nm) and surface coverage theories, established an adsorbed phase density upper limit of 0.36 g/mL, validating van der Waals density over liquid-phase density. Molecular simulations further reveal pressure-driven Langmuir-type increases in ρ_a and nonlinear temperature effects influenced by adsorption potential redistribution [36,37]. However, they fail to provide reliable density estimates due to the gap between simulations based on simplified pore models and real coal samples. Given coal's high heterogeneity, accurately reconstructing pore networks at the cross-scale and structural complexity is technically infeasible.

In this study, to avoid biases from non-physical based models and the challenges of reconstructing pore structures, we directly probed adsorption density using small-angle neutron scattering (SANS) by proposing a mechanical constrained scattering model. SANS is a versatile, non-invasive technique capable of characterizing pore sizes typical from 5 to 4000 Å [38]. Unlike NMR, which distinguishes adsorbed and free methane via hydrogen relaxation but is only sensitive at sufficient concentration levels, SANS probes scattering length density (SLD) fluctuations [39,40] between confined methane and the matrix across the entire pressure range and it is able to simultaneously reveal both pore structure and confined gas properties.

SANS has been extensively used to characterize sedimentary and igneous rocks, particularly in studying hierarchical pore morphology evolution under in situ conditions. It has provided insights into pore size distribution [41–44], porosity [45,46], pore accessibility [47–49], fractal dimension [42,50] in coal and shale. These structural characterizations form the foundation for understanding fluid storage and transport in porous media, linking pore-scale morphology to adsorption behaviors. Building on these structural insights, SANS has been applied in probing the confined gas phase properties within porous systems. Melnichenko et al. [51] was the first to apply SANS to differentiate bulk and confined CO_2 behavior, estimate fluid density in confined pores, and characterize CO_2 adsorption in Vycor glass and silica aerogels [52]. The findings revealed a highly densified adsorbed phase (~1.07–1.1 g/mL) that decreases with temperature, leading to further research on CO_2 adsorption. Based on SANS's superiority in characterizing the hydrogen element, hydrogen confinement has also been well studied. Gallego et al. [53] found that internal pore pressure could reach up to 50 times the external gas pressure, confirming the advantages of adsorptive over compressive hydrogen storage. He et al. [54] further investigated hydrogen adsorption in porous carbon, showing that hydrogen atoms preferentially adsorb in nanopores, achieving high density. Similarly, Bahadur et al. [55] demonstrated that micropore deformation is linked to adsorbed fluid density and revealed the strikingly different phase behavior of confined fluids (CO_2), with solvation pressures reaching up to 140 times the external pressure. These studies validated SANS's ability to derive confined fluid properties when appropriate models are applied. While research on methane adsorption on coal/shale remains limited [56,57], Eberle et al. bridged SANS-derived pore morphology with Fundamental Measure Density Functional Theory (FMDFT) to provide the first direct estimation of methane density within shale [50]. However, these estimations remain dependent on the external inputs to FMDFT. A more direct modeling approach is needed for improved robustness and reliability. Therefore, in this study, we investigate the mechanical response of the coal matrix to methane adsorption and then incorporate the mechanical constraint into the sphere scattering model to characterize the adsorption process.

This study pioneers a systematic investigation of methane storage in coal across a range of temperatures and pressures, an area previously unexplored in depth. Leveraging the proposed model, we employ SANS with CD_4 contrast matching [45,58,59] to overcome the limitations of traditional isotherm data and molecular simulations based approaches. By directly probing the SLD, which correlates with mass density, SANS provides more reliable insights into adsorption behavior as well as the adsorption induced morphology changes under varying methane pressures (400, 800, 1200, and 1600 psi) and temperatures (20, 50, 70, and 90 °C). To ensure a comprehensive and comparative analysis on the gas storage of coal reservoir, high-pressure volumetric methane adsorption measurements will be conducted under the same conditions to complement the SANS study. This approach provides a comprehensive understanding of the impact of adsorption phase density on methane storage in coal, offering valuable insights into both energy production and carbon sequestration.

2. Experimental work

2.1. Sample preparation and mineralogy

Pittsburgh coal bulk samples were sourced from Pittsburgh No. 8 coal seam, Pennsylvania, and pulverized using a crushing mortar to achieve a particle size range of 180–230 μm (60–80 mesh) for SANS and high-pressure volumetric methane adsorption measurements. Ultimate analysis revealed that the coal contains over 20 wt% volatile content, approximately 70 wt% carbon, and >80 wt% total organic carbon (TOC), classifying it as high-volatile bituminous coal (Table S1, Supporting information). Mineral compositions, as shown in Table 1, were determined via X-ray diffraction (XRD), with mineral densities obtained from the Mineralogy Database [60]. The mass fraction and chemical formula of TOC were estimated using a LECO carbon analyzer, and the TOC density was inferred from coal maceral densities in reference [61]. These chemical compositions and their corresponding mass density were

Table 1
Chemical composition and effective SLD of the Pittsburgh coal.

Composition	Density (g/cm^3)	Mass fraction (%)	SLD ($\times 10^{10}$ cm^{-2})
Poitevinite ($FeSO_4 \cdot H_2O$)	3.3	12.9	3.96
Pyrite (FeS_2)	5.0	3.1	3.81
Calcite ($CaCO_3$)	2.7	0.6	4.69
TOC ($C_{53.75}H_{41.11}O_{3.77}N_{0.67}S_{0.69}$)	1.4	83.5	2.53
Sample effective coherent SLD			2.77

then utilized to estimate the SLD of the coal matrix by [38]:

$$\rho^{*} = \frac{N_A d}{M} \sum_j p_j \left(\sum_i s_i \rho_i \right)_j \quad (2)$$

where ρ^* is the effective SLD, 10^{10} cm^{-2}, N_A is Avogadro's number, ρ is the physical density, g/mL, s_i is the proportion by the number of nuclei i in the compound j, p_j is the proportion by molecular number of the compound j in the mixture, and b_i is the coherent scattering for the nucleus i, 10^{10} cm^{-2}.

2.2. SANS experiments

SANS experiments were conducted on the General-Purpose Small-Angle Neutron Scattering Instrument (GP-SANS) at the High Flux Isotope Reactor (HFIR), Oak Ridge National Laboratory (ORNL), USA, using a 1 mm thick high-pressure cell (Fig. 1(a) and (b)) [62]. The raw data were corrected for the empty cell, detector efficiency, sample thickness, transmission, and instrument background, and were placed on an absolute intensity scale using a pre-calibrated standard with ORNL software. [63] Coal samples with aforementioned particle sizes of 180–230 μm were selected to optimize scattering across all pore orientations and reduce interference from interparticle voids as we used in our previous studies [49,64,65].

The SANS experiments utilized two neutron wavelengths: 4.75 Å, for measurements at sample-to-detector distances of 8.8 m and 1.1 m, and 12 Å, for measurements at 19.2 m. Transmission experiments were performed at 8.8 m and 19.2 m. The scattering vector Q covered a broad range from 0.0015 Å^{-1} and 0.77 Å^{-1}, corresponding to pore sizes from 4123 Å to 8 Å. Scattering under vacuum conditions was measured prior to CD_4 injection at temperatures of 20 °C, 50 °C, 70 °C, and 90 °C. At each temperature, CD_4 was injected incrementally at pressures of 400 psi, 800 psi, 1200 psi, and 1600 psi. ZAC or contrast matched conditions (where only signals from closed pores are detected) were achieved using CD_4 across all tested temperatures. Additionally, FTIR measurements were conducted under CH_4 and helium (He) atmospheres at those four temperatures (20, 50, 70, and 90 °C) to examine whether any decomposition of the coal matrix occurs.

2.3. High-pressure methane adsorption experiment

High-pressure methane adsorption experiments were conducted at the Geomechanics and Fluid Dynamics Lab, Pennsylvania State University. Isothermal volumetric adsorption capacities were determined at temperatures of 50 °C and 70 °C using the High-Pressure Adsorption System illustrated in Fig. 1(c) and (d). The same coal samples used in the SANS experiments were analyzed across six pressure steps, reaching a maximum pressure of approximately 1500 psi with methane.

3. Results and analyses

3.1. SANS profiles under vacuum condition

The raw data from the GP-SANS experiments have been corrected for empty-beam background scattering (Fig. S1). However, it is critical to note that residual background scattering primarily arises from the incoherent scattering contribution of hydrogen atoms, which exhibits isotropic distribution and remains constant across the entire scattering vector range Q. Analysis of the Porod plot (Fig. S1) revealed a pronounced linear relationship for $I(Q)Q^4$ in the high-Q region (Q > 0.1 Å^{-1}), confirming compliance with Porod's law. The incoherent background scattering was therefore estimated using the equation:

$$I(Q)Q^4 = C_{Porod} + I_{incoherent} Q^4 \quad (3)$$

The SANS profiles of the Pittsburgh coal sample under vacuum conditions, after background subtraction, are presented in Fig. 2. Across

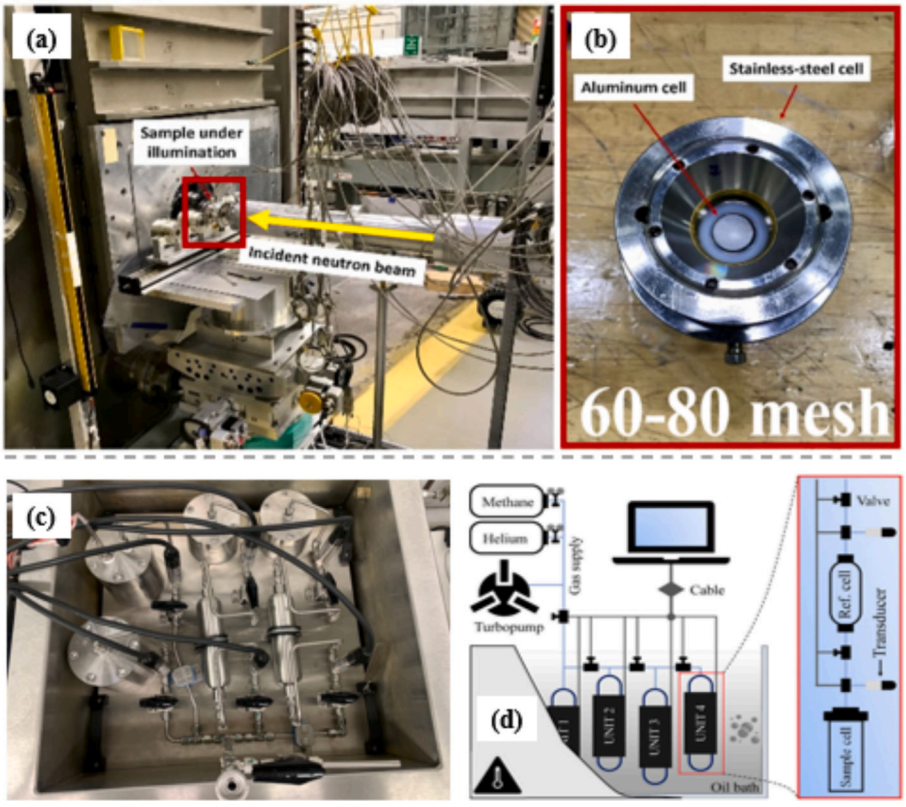

Fig. 1. Experimental setups. SANS: (a) Configuration of the General-Purpose GP-SANS Instrument at Oak Ridge National Laboratory; (b) 1 mm thick high-pressure cell used for sample containment. High-pressure Adsorption System: (c) laboratory image of the high-pressure adsorption system; (d) sorption system schematic.

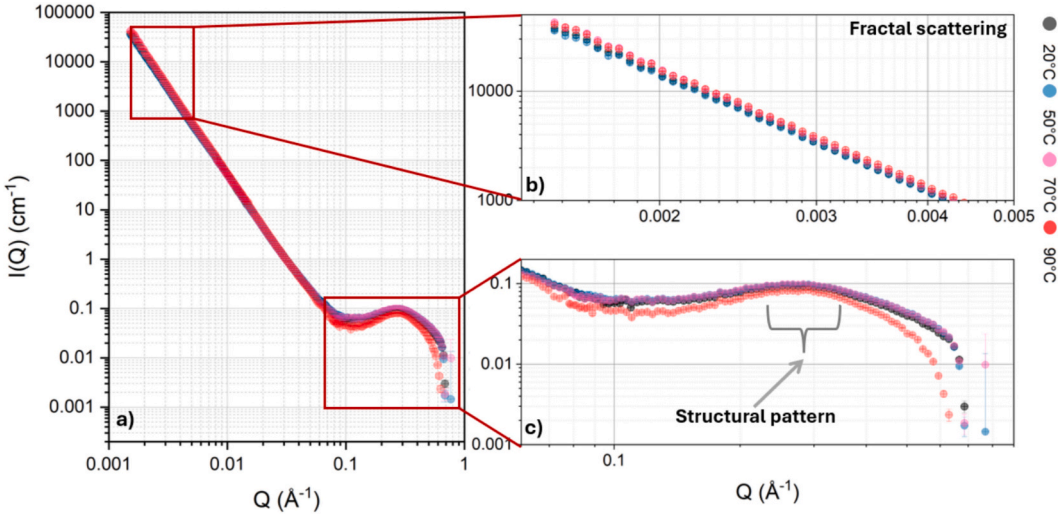

Fig. 2. SANS profiles of the Pittsburgh coal sample measured under vacuum conditions: (a) scattering profiles within the whole range; (b) low *Q* range scattering profiles; (c) high *Q* range scattering profiles.

the full *Q* range (Fig. 2a) the scattering curves at different temperatures exhibit consistency. However, temperature induced shifting is observed in both the low *Q* (0.0015–0.004 Å^{-1}), corresponding to pore sizes of 150–420 nm, length in real space $X \approx 2\pi/Q$) and high *Q* (>0.1 Å^{-1}), corresponding to pore sizes of <6.3 nm (Fig. 2b and c).

In the low *Q* regime, the scattering intensity initially decreases by approximately 15 % as the temperature rises from 20 °C to 50 °C, followed by a recovery and slight increase for 70 and 90 °C as shown in Fig. 2b. This non-monotonic behavior suggests thermally induced structural reorganization within submicron-scale pores, potentially involving hierarchical thermos-induced expansion and matrix reconfiguration. In the initial stage (20–50 °C), thermal expansion of surface-level macropores (e.g., fractures or open pores) induces geometric displacement of scattering volumes (Debye-Waller effect) [39], leading to intensity reduction; with temperature keeps going up (50 °C–70 °C/90 °C), pore expansion reach the limit and potential devolatilization or molecular rearrangement of coal organic matter at elevated temperatures could amplify pore-wall roughness [66,67], enhancing SLD contrast. While within the 20–90 °C window we studied, we did not observe a resolvable scattering change that would indicate thermal cracking; we therefore note that any such effect is below SANS detection and is left for future mechanical testing. In the high *Q* region, the intensity progressively increases with temperature up to 70 °C but declines at 90 °C, falling below the 20 °C baseline. The temperature-dependent increase in scattering intensity, particularly pronounced in the micropore region ($Q > 0.2$ Å^{-1}, pore sizes <3 nm). Under vacuum conditions, residual gases trapped in closed pores experience elevated pressure upon heating, leading to increased gas density and SLD. Concurrently, thermal expansion of the matrix induces localized compressive strain, further amplifying the SLD fluctuation. Temperature could also lower the surface-energy–controlled adsorption potential; wall asperities smooth out, and slit width contracts slightly, reducing adsorption space. Because SANS reflects ~10 nm width in this high *Q* region, even a small change in slit width is sufficient to produce the observed intensity loss, confirming that thermal compression, rather than macroscopic volumetric change, drives the signal. But it can be seen that the intensity increase is very subtle, which indicates limited contributions from residual gases (low gas density) within closed pores. The residual gas in coal has been reported to be low for coal. The reversal under 90 °C arise from a combination of gas escape from closed pores due to micropore fracturing at elevated temperatures (might be subtle) and matrix softening near the glass transition threshold of coal organic matters ($T_{g,coal}$~80–120 °C) [68,69]. FTIR spectra across 20, 50, and 70 °C show no significant differences between CH_4 and He environments. At 90 °C, however, subtle but distinguishable changes appear (Fig. S2), which are consistent with thermal softening near the glass transition temperature (*Tg*) of coal organic matter. Crucially, no new absorption bands are observed at any temperature, indicating that the coal matrix does not undergo chemical decomposition throughout the tested range. Additionally, the scattering hump observed in the high *Q* deviates from classical Porod or polydisperse sphere scattering behavior observed in most sedimentary and igneous rocks or carbon materials [38,45,49,50,53,56,65], suggesting nanoscale structural heterogeneities in the coal samples. These heterogeneities could be short-range ordered organic clusters such as localized alignment of aromatic clusters or aliphatic chains (~1–2 nm) or mineral-organic interfaces where nanoparticulate minerals (e.g., kaolinite, pyrite) embedded in the organic matrix introduce shape-factor modulation (e.g., spherical or lamellar structures), producing shoulder peaks [70,71].

The SANS profiles under vacuum conditions reveal that temperature variations can induce structural modifications in coal matrices, even in the absence of sorptive gases. Notably, these effects are predominantly localized within micropore regions (< 3 nm). Unlike typical sedimentary or igneous rocks, coal exhibits nanoscale heterogeneities that could significantly influence gas storage. Therefore, careful consideration is essential when analyzing the microstructure of coal.

3.2. SANS profiles after CD_4 injection

Fig. 3 presents the SANS scattering profiles of the Pittsburgh coal samples under CD_4 injection, demonstrating how sorptive gases, along with temperature, influence the scattering behavior of the system.

In Fig. 3, for all four temperatures, two main effects emerge. First, in the high *Q* region, the intensity differences among the various pressures (vacuum/0 psi, 400 psi, 800 psi, 1200 psi and 1600 psi) progressively diminish with increasing temperature, indicating that thermal nanoscale structural heterogeneity decrease suppresses the pressure-dependent adsorption in micropores. Thus, at 90 °C, the curves from different pressures converge more closely; the wider span of intensity difference in lower temperatures, especially 20 °C, means pressure has a more profound effect to regulate the micropore's SLD difference fluctuation at these conditions. Secondly, Fig. 3 highlights a distinct "ZAC failure point" in the high *Q* regime, where the ZAC (contrast-matched) curve ceases to show the expected minimum scattering and instead converges with or even exceeds the intensities of the lower-pressure curves. At low *Q*, the ZAC condition successfully reduces scattering by offsetting the

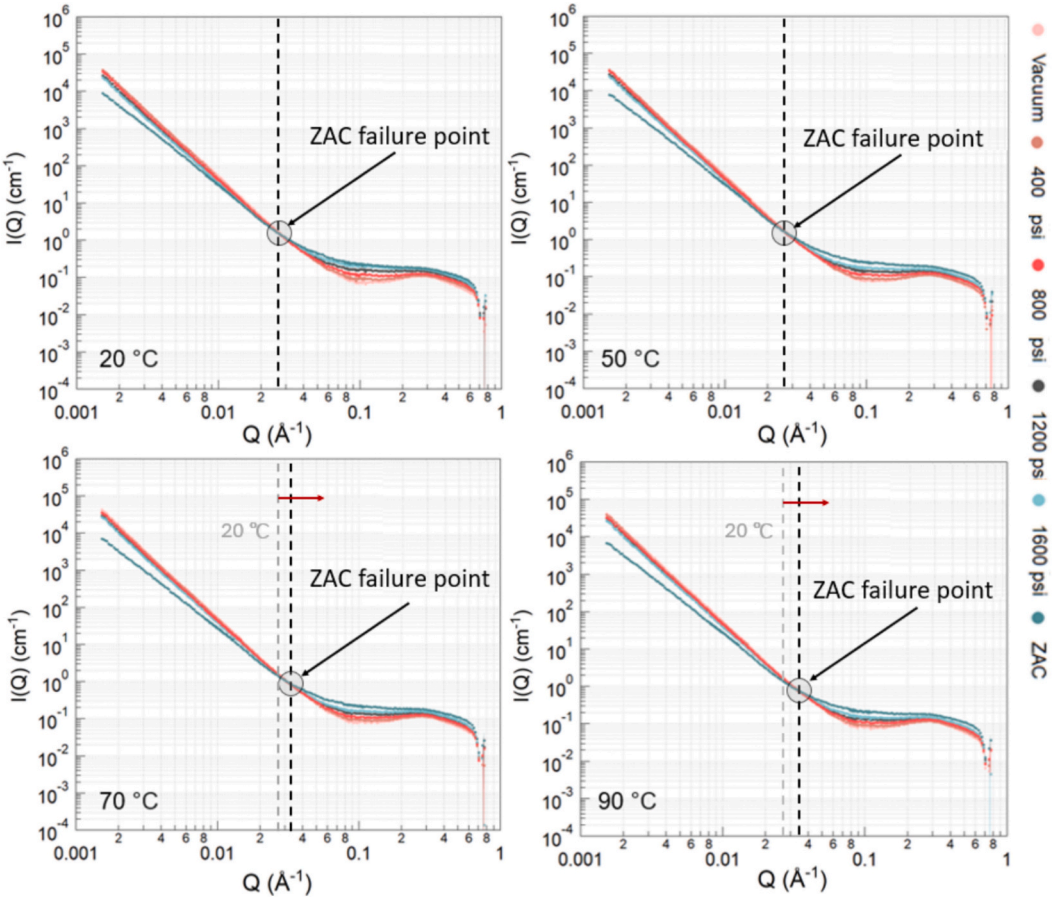

Fig. 3. SANS scattering profiles of the Pittsburgh coal sample measured at various temperatures under different CD_4 injection pressures.

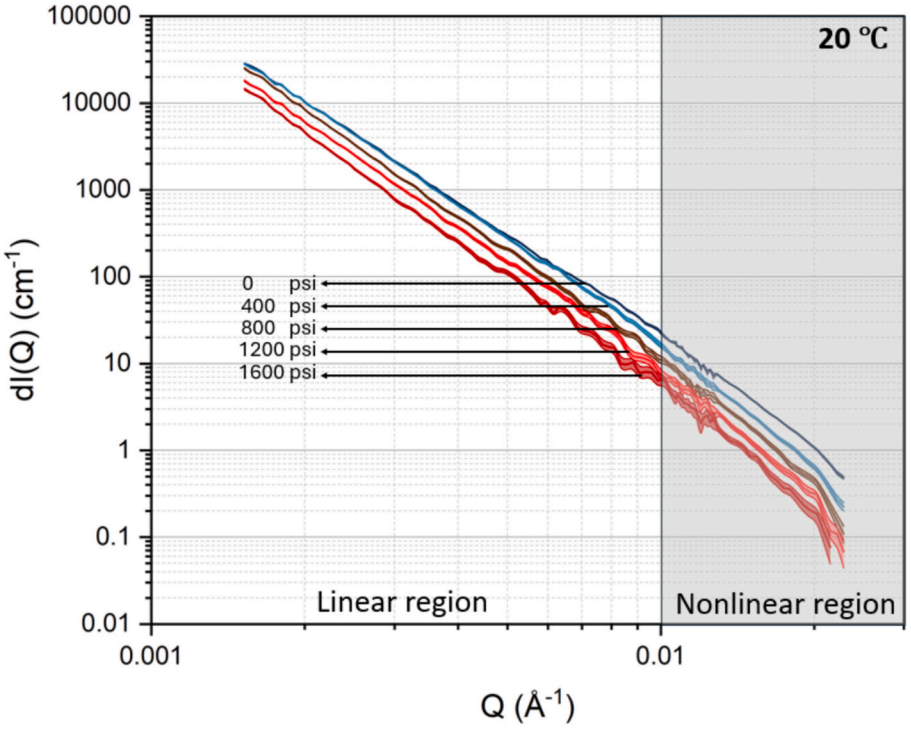

Fig. 4. SANS intensity difference between various pressures and the ZAC condition, 20 °C.

coal matrix SLD based on CD_4 bulk fluid density. However, upon reaching the ZAC failure point (pore size <20 nm), the local density of CD_4 within these pores apparently surpasses that of the coal matrix, disrupting the intended contrast match. This local densification arises from enhanced adsorption or partial condensation in micropores where the fluid experiences stronger pore–wall interactions, thus driving the SLD above its bulk pressure-based design value if assuming pure gaseous phase. As temperature increases from 20 °C to 90 °C, the ZAC failure point shifts toward higher Q, indicating that elevated temperatures suppress fluid condensation in pores, requiring smaller pore sizes (i.e., higher Q) to achieve the same local CD_4 densification. Consequently, at higher temperatures, the mismatch between CD_4 and the coal matrix SLD emerges only at increasingly smaller real length scales. This observation underscores the interplay among temperature, pore-size distribution, and adsorbed-phase density: while the ZAC approach remains valid at lower Q where adsorption effects are weaker, its efficacy diminishes in the micropore regime, where local condensation invalidates the bulk-density assumption. Such insights render a single ZAC setting insufficient across the entire Q range.

The pressure induced SLD contrast has an apparent decrease in low Q as shown in Fig. 4 20 °C as an example. By comparing the intensity difference, $dI(Q) = I(Q) - I(Q)_{ZAC}$, it is worth investigating other pressures to ZAC condition to further investigate the pore wall effect on adsorption. At low $Q < 0.01$ Å^{-1}, the difference curves for these various pressures shift almost linearly relative to the ZAC baseline, indicating that the increased CD_4 pressure uniformly reduces scattering in larger pores. In other words, under these conditions, the fluid's bulk density assumption still holds, and contrast matching remains largely effective. It also demonstrated that the adsorbed as is negligible compared to the freely compressed free gas and thus it does not play a observable role in free phase SLD estimation. However, once Q exceeds approximately 0.01 Å^{-1} (the boundary of the "nonlinear region" in Fig. 4), deviations from linearity become evident. While at $Q > 0.01$ Å^{-1}, prior to reaching the ZAC failure point, the deviation from linearity suggests that adsorption effects have already altered the local CD_4 density relative to the bulk-density assumption. Closer attention should be given while analyzing the scattering data before and after entering the condensation region where deviation from linearity occurs.

3.3. Adsorption induced coal microstructure alteration

Prior to any SLD-based analysis, it is essential to first characterize how the sample's structure responds to changes in adsorption pressure and temperature, providing a baseline and guiding subsequent SLD-based evaluations as key prior information—a critical step in SANS data interpretation. To achieve this, we directly processed the scattering data by performing a Fourier transform on the measured intensity, thereby obtaining the real-space correlation functions (CF) and the corresponding 1D and 3D correlation factors $\Gamma_1$and Γ_3, respectively:

$$\Gamma_1(X) = \frac{1}{Q^*}\int_0^\infty I(Q)Q^2\cos(QX)dQ \tag{4}$$

$$\Gamma_3(X) = \frac{1}{Q^*}\int_0^\infty I(Q)Q^2\frac{\sin(QX)}{QZ}dQ \tag{5}$$

$$Q^* = \int_0^\infty I(Q)Q^2dQ \tag{6}$$

The CF results for scattering under vacuum are shown in Fig. 5, providing a baseline that captures the coal matrix's intrinsic structural motifs in the absence of sorbed gases. Across all temperatures, the CFs exhibit a broadly similar pattern, suggesting that thermal effects remain relatively modest in this range. Notably, the 1D correlation function features a prominent peak near 14 Å, consistent with short-range ordered, lamellar-like organic clusters. In contrast, the 3D correlation function shows fewer discernible peaks, which is likely due to orientational averaging inherent in analyzing powdered samples. In disordered coals, polyaromatic domains can exhibit local layering or turbostratic arrangements that do not conform to the well-defined planes observed in crystalline graphite [71]. Consequently, these features could be more appropriately described as lamellar-like or quasi-stacked (referred to as "lamellar spacing" in this study for convenience). Nonetheless, the consistent ~14 Å peak supports the presence of partially stacked aromatic ring systems, aligning with diffraction-like scattering observed in certain semi-graphitic carbonaceous materials at similar spacings [56]. Closer inspection reveals a slight reduction of approximately 0.16 Å in the lamellar spacing at 50 °C and 70 °C compared with 20 °C, followed by an increase of 0.081 Å at 90 °C. This observation supports our previous assumption that, below 90 °C, thermal expansion exerts localized compressive strain on the organic matrix, thereby decreasing interlayer distances. Once the temperature reaches 90 °C, partial matrix softening (possibly near the glass transition region) allows for a minor rebound in

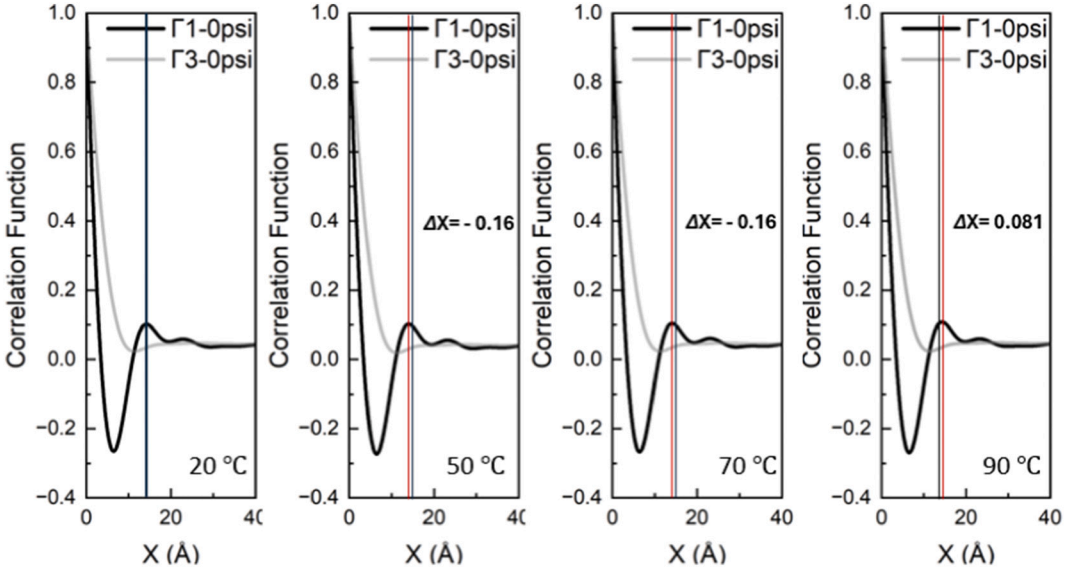

Fig. 5. Length scales and recurring motifs within the coal matrix.

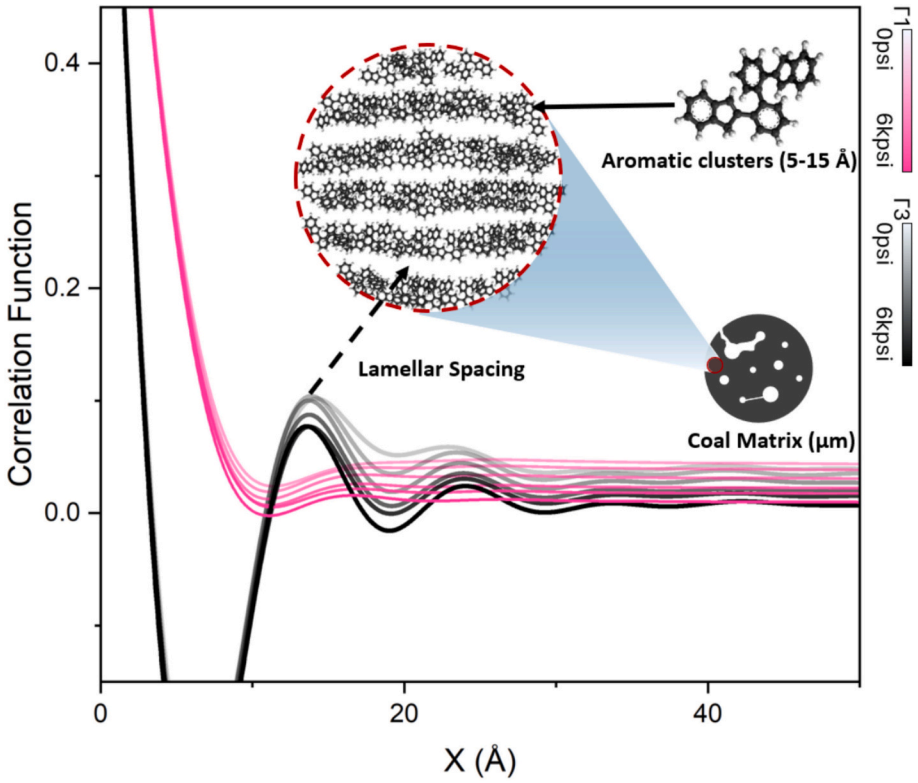

Fig. 6. Lamellar spacing alteration under varying gas pressure, 20 °C.

lamellar spacing.

Fig. 6 presents the CF results for SANS under varying gas pressures at 20 °C. As lamellar spacing responds consistently to changing gas pressure at a given temperature, the CF results for other temperatures are provided in Fig. S3. By comparing the peak positions under different pressures, one can discern shifts in the interlayer lamellar spacing and local structural reorganization—effects likely arising from the interplay between matrix elasticity and fluid adsorption. For instance, at higher pressures, an increased fluid density by pressure increase will ultimately and inevitably contract the molecular structure of organic components like aromatic layers or partially infiltrate interlayer gaps, thus reducing the characteristic spacing and altering the peak profile.

Fig. 6 presents the real-space CFs under various gas pressures at 20 °C, highlighting how lamellar spacing in the coal matrix responds to increasing external pressure. As lamellar spacing responds consistently to changing gas pressure at a given temperature, the CF results for other temperatures are provided in Fig. S3. The CF peaks, typically observed between 10 and 20 Å, align with the characteristic length scale of aromatic clusters. As depicted in the coal matrix illustration in Fig. 6, increasing pressure shifts the peak position to smaller separations, indicating a contraction of aromatic layers or domains. One possible explanation is the mechanical strain imposed by higher gas pressure, which compresses the matrix and reduces interlayer spacings [72]. Additionally, fluid infiltration into interlayer gaps, particularly in microporous regions, may promote partial layer collapse or bridge void spaces between aromatic sheets, lowering the surface potential and

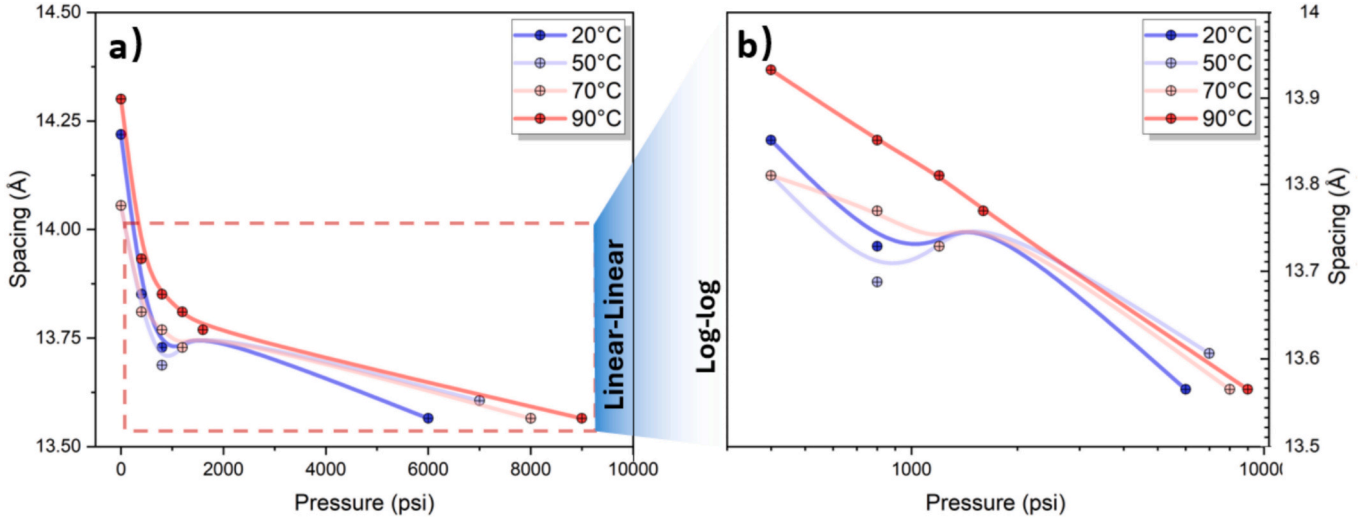

Fig. 7. Variations in lamellar spacing under varying external gas pressure.

drawing them closer together.

This pressure-induced compaction supports the assumption that coal's organic matrix exhibits elastic behavior to at nanoscale deformation. To further examine these effects, changes in lamellar spacing under varying gas pressure are analyzed, with the results presented in Fig. 7. It can be observed that across all temperatures, lamellar spacing decreases rapidly upon initial pressure increase, but the rate of decrease significantly slows at higher pressures. When rescaled on a log-log scale (Fig. 7b), the data exhibit a near-linear relationship between lamellar spacing and external gas pressure, reinforcing the idea that coal's organic matrix can undergo controlled nanoscale elastic deformation. Given the consistent trend across different temperatures, the lamellar spacing values at each pressure are averaged to derive the following power-law-type relationship, as shown in Fig. S4:

$$S = p^{-0.00377} e^{1.14969} \tag{7}$$

This regression indicates that while the matrix compacts more rapidly at lower pressures, it becomes progressively less compressible as pressure increases [73]. Moving forward, this relationship will serve as a key constraint in subsequent SLD-based analyses, providing a foundational framework for modeling inputs. The correlation function analysis highlights the dynamic nature of coal's microstructure under varying pressure and temperature. These findings suggest that external gas pressure can reconfigure aromatic domains in coal, impacting gas storage capacity, transport properties, and matrix stability, an important reality consideration for related studies.

4. Discussion

4.1. Gas accessibility model under external pressure

As widely recognized in the porous media characterization community, porosity measurements vary depending on the probing gas used. This discrepancy arises from differences in gas accessibility under specific external pressure conditions. Gas accessibility is also a key factor in accurately estimating the in-place gas content. In this study, we introduce a novel approach for determining gas accessibility directly from SANS data without the need for fitting, providing a more direct and model-independent assessment of pore accessibility under varying conditions.

In a multiphase system, the SANS scattering invariant Q^* is closely related to the volume fractions of the different phases and the contrast between their SLDs. For a two-phase system, the invariant is typically expressed as

$$Q^* = \int_0^\infty I(Q)Q^2 dQ = 2\pi^2\phi(1-\phi)\Delta\rho^{*2} \tag{8}$$

Assume that system consists of coal matrix and pores. Under vacuum conditions, the pores contain no gas, while under adsorption conditions, the pores are partially filled with gas. In the pores, let $f\,(0 \le f \le 1)$ be the volume fraction of the pore space that is filled with gas (i.e., the accessibility). Under adsorption conditions, the effective SLD in the pores becomes

$$\rho^*_{pore,eff} = f\cdot\rho^*_{CD_4} + (1-f)\cdot\rho^*_{VAC} \tag{9}$$

where $\rho^*_{CD_4}$ is the SLD of CD_4 in pores, 10^{10} cm^{-2}, ρ^*_{VAC} is the SLD of empty pores, 10^{10} cm^{-2}.

Thus, for the two-phase model (coal matrix vs. pores), the scattering invariant of the entire system is

$$Q^* = 2\pi^2\phi(1-\phi)\left(\rho^*_m - \rho^*_{pore,eff}\right)^2 \tag{10}$$

where ρ^*_m is the SLD of the solid matrix.

The invariant can be more specifically written in the following conditions: when the pores are under vacuum ($f = 0$) and partially filled with CD_4 ($f > 0$).

$$\begin{aligned} Q^* &= 2\pi^2\phi(1-\phi)\left(\rho^*_m - \rho^*_{VAC}\right)^2 \quad f = 0 \\ Q^* &= 2\pi^2\phi(1-\phi)\left[\rho^*_m - \left(f\cdot\rho^*_{CD_4} + (1-f)\cdot\rho^*_{VAC}\right)\right]^2 \quad f > 0 \end{aligned} \tag{11}$$

For coal, which has a very low porosity of approximately ~2–5 %, the production of $\phi(1-\phi)$ remains relatively stable even with subtle variations in porosity. Therefore, in this analysis, we assume that $\phi(1-\phi)$ remains constant. This will further reduce Eq. (11), and the comparison between these two conditions will lead to

$$\frac{Q^*_p}{Q^*_{VAC}} = \left(\frac{\rho^*_m - \left(f\cdot\rho^*_{CD_4} + (1-f)\cdot\rho^*_{VAC}\right)}{\rho^*_m - \rho^*_{VAC}}\right)^2 \tag{12}$$

Rearrange the Eq. (12) to get

$$f = \left|1 - \sqrt{\frac{Q^*_p}{Q^*_{VAC}}}\right| \frac{\rho^*_m - \rho^*_{VAC}}{\rho^*_{CD_4} - \rho^*_{VAC}} \tag{13}$$

Because $\rho^*_{pore,eff}$ is what we could estimate by SANS data analysis, thus by substituting $\rho^*_{CD_4} = \left(\rho^*_{pore,eff} - (1-f)\cdot\rho^*_{VAC}\right)/f$into Eq. (13) and let $\rho^*_{VAC} = 0$, we get

$$f^2 = \left|1 - \sqrt{\frac{Q^*_p}{Q^*_{VAC}}}\right| \frac{\rho^*_m}{\rho^*_{pore,eff}} \tag{14}$$

This method will be applied in later chapters based on the estimated gas density.

4.2. Estimation of confined gas density

Once the ability of external gas pressure to alter the coal nanostructure and impact various gas storage related processes is established, the next critical step is to quantify the magnitude of these effects. Central to this analysis is the accurate estimation of gas density, a key correction parameter for precisely determining gas adsorption capacity [16]. In the coal matrix, gas is stored in two distinct confined phases: free gas within fractures or macro/mesopores at the micron to sub-micron scale, and as adsorbed gas within micropores and nanopores, where molecular interactions with the pore walls significantly alter local density and thermodynamic behavior as discussed previously.

4.2.1. Confined gas density in macropores and mesopores

Scattering intensity contributed from the pores for a two-phase system is proportional to the contrast factor k_n:

$$I(Q) \propto k_n = (\Delta\rho^*)^2[\phi(1-\phi)]_Q \tag{15}$$

According to Eq. (15), the ratio between the scattering intensity of the samples under CD_4 injection and under vacuum condition can be represented as

$$\frac{I_{CD_4}(Q)}{I_{vac}(Q)} = \frac{\left(\Delta\rho^*_{CD_4}\right)^2[\phi(1-\phi)]_Q}{\left(\Delta\rho^*_{vac}\right)^2[\phi(1-\phi)]_Q} \tag{16}$$

where $\Delta\rho^*_{CD_4}$ and $\Delta\rho^*_{vac}$ are the SLD differences under CD_4 injection and vacuum conditions, respectively. Here, we assume that the CD_4 has total open pore accessibility to fractures or macro/mesopores and the pore volume fraction remains unchanged between vacuum and CD_4 injection conditions. This assumption is reasonable because, although gas molecules can be adsorbed onto pore surfaces or diffuse into the matrix, the total available pore space in fractures or macro/mesopores remains largely stable in the absence of significant structural deformation or collapse in this region. Additionally, since the SLD of pores under vacuum conditions is effectively zero. Thus Eq. (15) can be further reduced to

$$\frac{I_{CD_4}(Q)}{I_{vac}(Q)} = \left(\frac{\rho_m^* - \rho_{CD_4}^*}{\rho_m^*}\right)^2 \quad (17)$$

Gas density and SLD for CD_4 have empirical relation:

$$\rho_{CD4}^* = 10\rho_{CD4} \times 10^{10}\text{cm/g} \quad (18)$$

whereρ_{CD_4} is the mass density of CD_4, and $\rho_{CD_4} = 1.25 \times \rho_{CH_4}$.

When $\rho_m^* > \rho_{CD_4}^*$, corresponding to the region before the ZAC failure threshold (Fig. 3), Eqs. (17) and (18) can be combined to estimate the confined gas density as a function of the scattering vector Q in this size region. As previously discussed, this region primarily corresponds to pore sizes >20 nm (macro-/mesopores), where the influence of pore wall effects is less pronounced. However, before applying Eq. (17), it is important to subtract the intensities of the vacuum and CD_4 injected conditions using the ZAC intensity at each individual Q. This step is necessary to eliminate the contribution from closed pores, and SLD fluctuations in coal matrix, especially those organic matter-mineral interfaces. This approach is also only valid before the ZAC failure threshold (macro/mesopores region). As shown in Fig. 4, beyond this threshold, the subtracted intensity becomes negative, indicating that the ZAC correction is no longer applicable due to deviations in the designed contrast matching SLD.

The CH_4 density estimation results in macro and mesopores are shown in Fig. 8. It is obvious that below $Q = 0.01$ Å^{-1}, the estimated in-pore CH_4 densities remain relatively constant and closely match the bulk density at each respective temperature. This agreement indicates that, for pore sizes larger than roughly 60 nm, the CH_4 behaves essentially like a compressed gas with minimal pore-wall effect; this agreement also supports the validity of the present density estimation approach in the macro/mesopore regime. Consistent with Fig. 4, once Q exceeds 0.01 Å^{-1} (indicating entry into the smaller pore region, denoted in Fig. 4 as the onset of nonlinearity), the estimated densities surge sharply, surpassing the corresponding bulk densities by up to several multiples. Such surge suggests that, in pores below about 60 nm, confinement and capillary-condensation like effects become significant, elevating the local fluid density above what would be expected from simple bulk compression. These findings align well with classical descriptions of pore condensation governed by the Kelvin equation in mesopores [74]. As pore diameters decrease, the increased curvature of the gas–liquid meniscus can lead to enhanced local pressures (or equivalently lowered chemical potentials), driving partial condensation at pressures below the macroscopic saturation pressure. Although CH_4 remains supercritical under the tested conditions, forming a true liquid phase may not be possible. However, similar mechanistic effects, such as enhanced adsorption and densification due to confinement, must be considered to explain the observed density surge.

From a methodological standpoint, the stable match between the estimated and bulk densities at low Q provides confidence that the scattering density-based method is robust in the macro/mesopore range. Meanwhile, the distinct nonlinear jump beyond the condensation region as shown in Fig. 8 underscores the importance of accounting for confinement when interpreting SANS data in the micropore regime.

4.2.2. Adsorbed gas density in micropores

To overcome the limitations of the model-independent approach and effectively account for the nanoscale structure, we apply a sphere-based model to extract detailed structural information in the high Q region. This model enables a more precise characterization of micropore scale features where direct density retrieval is not feasible. Additionally, to capture the scattering contributions from interparticle interactions and fracture related structures at low Q, a power-law model will be incorporated. This combined modeling approach ensures a more comprehensive interpretation of the SANS data across different pore size regimes:

$$I(Q) = C_p Q^{-\alpha} + \phi\left(\Delta\rho^*_{CD_4,micro}\right)^2 \int P(Q,r)S(Q,r)D(r)dr + I_{incoherent} \quad (19)$$

where the $P(Q,r)$ is the form factor for a sphere.

$$P(Q,r) = \left[\frac{3(\sin(Qr) - Qr\cos(Qr))}{(Qr)^3}\right]^2 \quad (20)$$

and $S(Q,r)$ is structure factor, accounting for interparticle interactions,

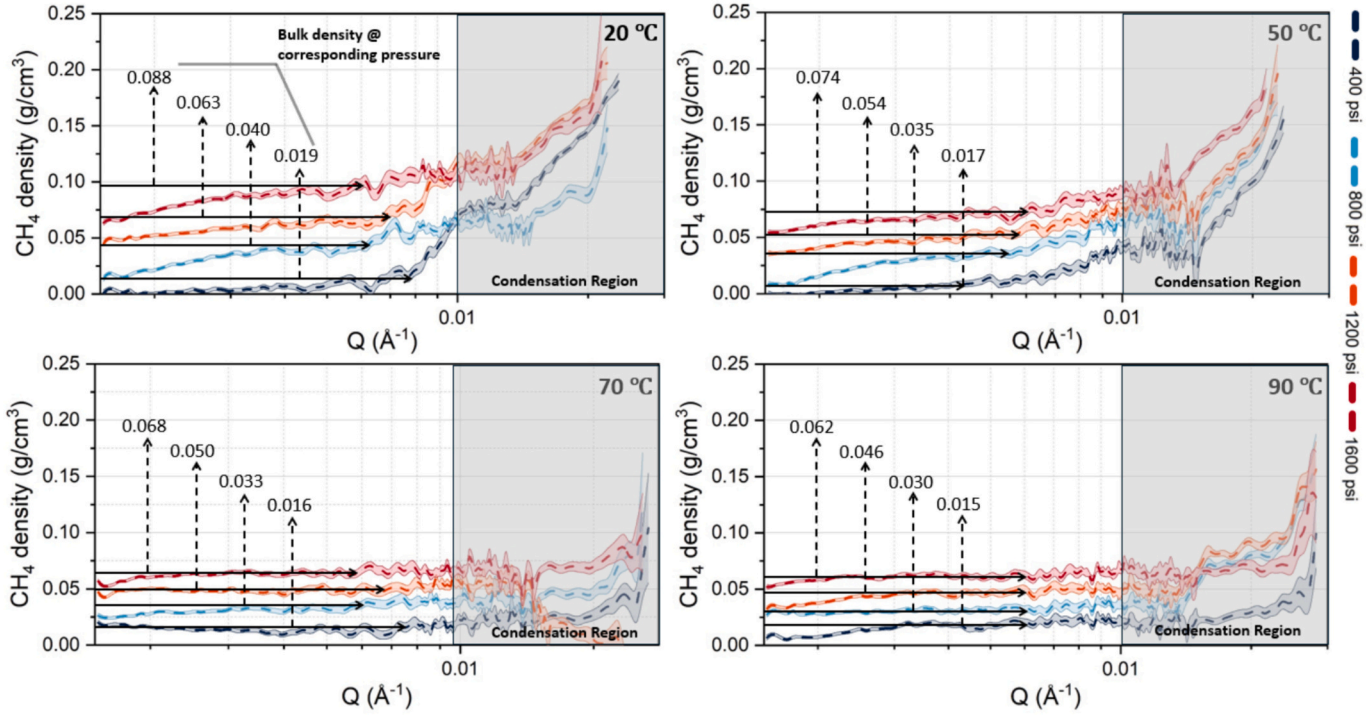

Fig. 8. Estimation of CH_4 density in macro and mesopores.

regarding dilute pore distribution in coal matrix, it is taken the value of one, $D(r)$ is the size distribution function describing the probability of finding a sphere with radius r, here we use the lognormal distribution to describe the natural rock.

$$D(r) = \frac{1}{r\sigma\sqrt{2\pi}} e^{\frac{-(\ln r - \ln r_m)^2}{2\sigma^2}} \tag{21}$$

where σ and r_m are the standard deviation and mean of the distribution. The incoherent scattering was removed using Eq. (5). Here by incorporating pressure induced nano structural alterations expressed in Eq. (7).

$$r_m = r_0 \left(\frac{p}{p_0}\right)^{-0.00377} \tag{22}$$

Here, r_0 represents the mean pore size under vacuum conditions, where the SLD contrast between the matrix and the pore is most readily determined, as it directly equals the SLD of the matrix. Therefore, r_0 is chosen as the baseline for comparison. Additionally, p_0 denotes the pressure under vacuum conditions, which is set to 0.1 psi to reflect a realistic experimental scenario.

Eq. (19) was then used to model the experimentally obtained SANS data. However, as shown in Fig. S5(a), the pure polydisperse sphere model alone is insufficient to fully capture the high Q scattering behavior. Thus, to better capture the high Q scattering behavior, we further incorporate a Gaussian peak scattering model to account for the contribution of short-range ordered organic clusters, as previously discussed:

$$I(Q) = C_p Q^{-\alpha} + \phi\left(\Delta p^*_{CD_4,micro}\right)^2 \int P(Q,r)S(Q,r) \left(\frac{1}{r\sigma\sqrt{2\pi}} e^{\frac{-\left(\ln r - \ln r_0 \left(\frac{p}{p_0}\right)^{-0.00377}\right)^2}{2\sigma^2}} \right) dr + I_G e^{\left(\frac{-(Q-Q_0)^2}{2(\sigma_G)^2}\right)} + I_{incoherent} \tag{23}$$

where Q_0 is the peak position, σ_G is the peak width.

As seen in Fig. S5(b), incorporating a Gaussian peak term into the model significantly improves the fit to the data in the high Q region. The methane density confined in micropores was estimated using Eq. (23), with results summarized in Table 2. The data indicates that under each temperature condition, the confined density generally increases with rising external pressure. However, at a fixed pressure, the density remains relatively stable despite temperature variations. Fig. 8 further illustrates the relationship between confined density and external pressure, where density values across all tested temperatures were averaged at pressure levels. A similar averaging approach was applied to the ratio of effective bulk pressure to actual external pressure. As for the effect of wall roughness on density, Fig. S6 shows that the non-monotonic behavior of the surface fractal dimension ($Ds = 6 - \alpha$) across pressures means that a universal Ds–adsorption capacity relationship cannot yet be established.

Fig. 9a illustrates the confined methane density within micropores shows a positive correlation with increasing external pressure. Specifically, during the initial loading phase, the density increase is rapid, indicating a strong response of the adsorbed gas to the applied pressure. However, as external pressure continues to rise, the rate of increase in confined methane density diminishes, suggesting a saturation effect as the micropore approaches its storage limit under higher pressures. Furthermore, the estimated maximum density is lower than both the liquid and van der Waals densities (as shown in Fig. 9a), as well as our previously proposed theoretical limit of 0.36 g/mL [76]. Conversely, the ratio of effective micropore pressure to external pressure exhibits an inverse trend. At low external pressures, Rp reaches values as high as 26.9, indicating a significant pressure amplification within the micropores. This amplification highlights the ability of adsorption potential within micropores to act as a "compressor," concentrating methane gas to pressures significantly greater than the bulk external pressure. Such behavior emphasizes the micropores' energy storage capacity, where the substantial pressure differential reflects the high adsorption potential energy within the confined system. This has critical implications in evaluating coal outburst hazards, as the release of stored energy from micropores could contribute significantly to the dynamics of sudden gas release during an outburst event. However, as external pressure increases, the rapid decline in Rp suggests that the compression effect becomes less pronounced. This is likely due to the external gas undergoing further compression, reducing the relative contribution of the micropore's adsorption potential to the overall pressure. This diminishing ratio at high pressures indicates a transition toward equilibrium conditions, where the internal and external pressures become more aligned.

In engineering applications, these findings highlight the dual role of micropores: as both storage systems and energy reservoirs. The capacity of micropores to store methane under elevated pressure conditions makes them valuable for natural gas storage and sequestration applications. Simultaneously, the release of stored energy from these micropores poses a significant safety risk in mining operations, underscoring the need to monitor and model these pressure-dependent behaviors. Following the estimation of confined methane density within micropores, the accessibility of these pores can be estimated through the application of the proposed model, expressed in Eq. (14). The results, as presented in Fig. 9b, are average over temperature,

Table 2
Estimated adsorbed CH_4 density in micropores.

Temperature (°C)	$p_{external}$ (psi)	ρ_{CH4} g/mL	$p_{bulk,eff}$* (psi)	$Rp = p_{bulk,eff}$ / $p_{external}$
	400	0.274	7000	17.5
	800	0.286	7875	9.9
20	1200	0.290	8250	6.9
	1600	0.305	9541	6.0
	ZAC(6000)	0.305	9458	1.6
	400	0.27	8750	21.9
	800	0.280	9208	11.51
50	1200	0.282	9416	7.8
	1600	0.29	9666	6.0
	ZAC(7000)	0.289	11,292	1.4
	400	0.276	10,042	25.1
	800	0.286	10,917	13.6
70	1200	0.289	11,167	9.3
	1600	0.290	11,417	7.1
	ZAC(8000)	0.290	11,292	1.4
	400	0.271	10,750	26.9
	800	0.272	10,792	13.5
90	1200	0.274	11,000	9.7
	1600	0.263	9916	6.2
	ZAC(9000)	0.284	11,958	1.3

$p_{bulk,eff}$: the bulk pressure corresponds to the estimated density in bulk phase. From NIST Standard Reference Database 69 [75].

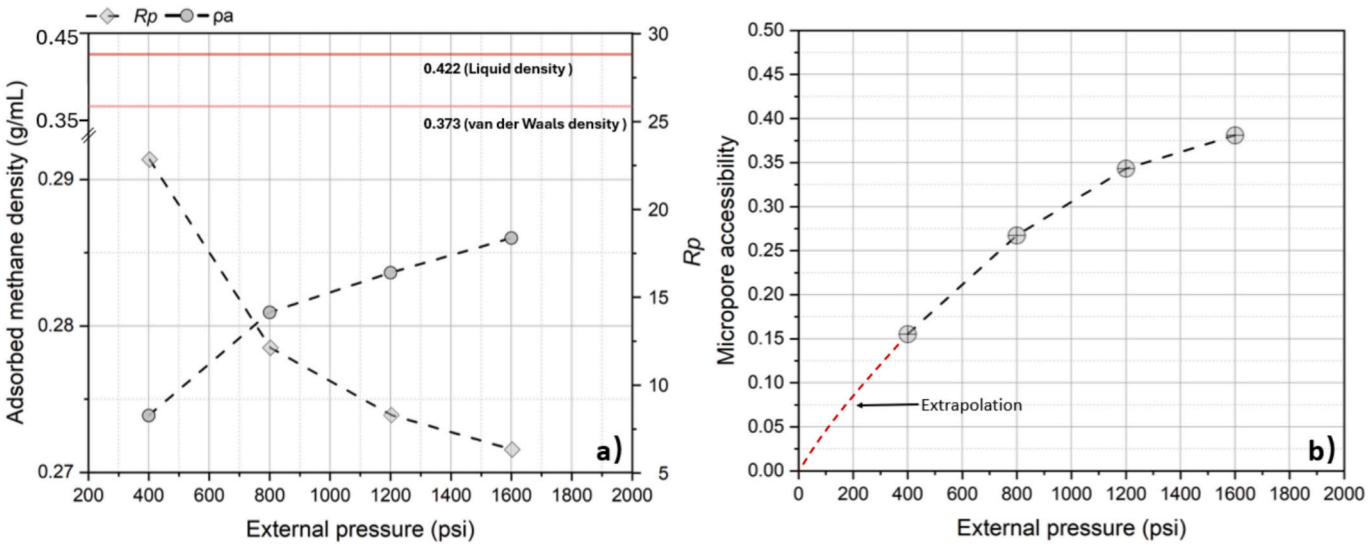

Fig. 9. a) Estimation of adsorbed CH_4 density in micropores; b) micropore pore accessibility in various pressures.

revealing a positive correlation between micropore accessibility and external pressure. As the external pressure increases, micropore accessibility demonstrates a steady rise, indicating that higher pressures enhance the effective utilization of micropore storage capacity. Extrapolation of the modeled trendline to vacuum conditions confirms that micropore accessibility approaches zero under zero external pressure. This behavior is consistent with the theoretical framework, as the absence of external pressure eliminates the driving force necessary for gas molecules to penetrate micropores. The extrapolated result underscores the mathematical rigor of the proposed model, providing a robust foundation for understanding micropore behavior across a range of pressure conditions. The accessibility values obtained align closely with findings from our prior studies, reinforcing the model's validity and applicability. Notably, the gradual saturation trend observed at higher pressures suggests that micropores approach their maximum accessibility threshold as pressure increases. This trend reflects the physical limitations imposed by the pore structure and the rest inaccessible part should be the closed pores.

In conclusion, the proposed model effectively captures the relationship between external pressure and micropore accessibility, providing a theoretical and practical basis for further investigations into gas adsorption and storage mechanisms in microporous materials.

4.3. Implication on methane storage and environmental relevance

As mentioned earlier, gas density in adsorbed phase is crucial for determining adsorption capacity, particularly for converting gas storage from GSE. The estimated CH_4 density is used in Eq. (1) to obtain the absolute adsorption amount. As shown in Fig. 10, the results from the high-pressure methane adsorption experiments (described in Section 2.3) demonstrate that using the liquid methane density (using as an upper cap compared to van der Waals density) as a correction parameter leads to an underestimation of the adsorption capacity of this coal sample. This is because the density of adsorbed methane, estimated via SANS, is smaller than the liquid methane density. Such a result is consistent with theoretical expectations, as methane in micropores, even under the influence of adsorption forces, cannot reach the density of liquid methane due to its supercritical nature under the experimental conditions. The adsorbed methane density is physically constrained by the combination of supercritical gas behavior and the spatial confinement effects of micropores. The adsorption potential within micropores enhances the local methane density compared to the bulk phase but cannot reach liquid-like densities due to the thermodynamic limitations of supercritical methane. By incorporating SANS-derived confined density values, this study achieves a more realistic correction of

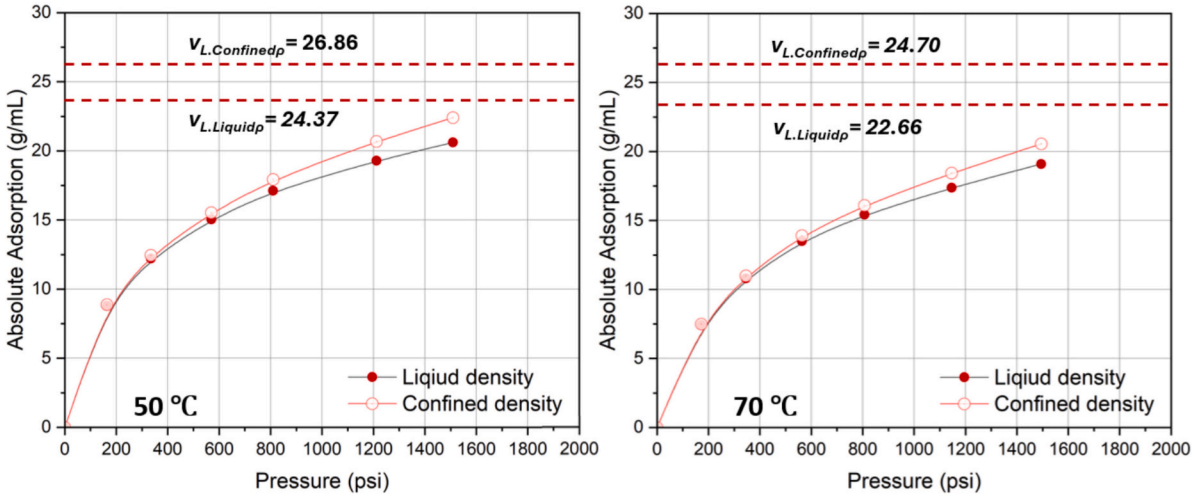

Fig. 10. Absolute adsorption amount correction using two methane density in micropores.

adsorption capacity. The corrected results should provide a more accurate representation of the coal's true sorption capacity, highlighting significant differences between Langmuir Volumes at 50 °C and 70 °C. Notably, as pressure increases, the gap between these densities widens, further emphasizing the necessity of adsorbed density corrections at elevated pressures.

From an environmental/energy strategy point of view, our refined density correction changes the estimated sorptive capacity by up to ~10 % at reservoir pressures, a deviation large enough to alter greenhouse-gas inventory factors and to shift the economic break-even for CO_2-ECBM or CCS projects. Furthermore, the pronounced pressure amplification we observe in micropores (up to 27-fold at 90 °C) implies that sudden pressure drops—such as those accompanying mine-wall failure—can liberate far more CH_4 than models using liquid-density corrections predict, an insight directly relevant to outburst-risk assessment. Because once the compression factor could be measured in situ, it could be incorporated into a real-time early-warning protocol: an abrupt rise in the factor would flag places where stored elastic energy is nearing a critical threshold for gas outburst.

Additionally, diffusivities across various measurement windows were derived using the approach introduced in our previous work [77]. In contrast to the pronounced discrepancies in adsorption amounts caused by applying two different methane densities, the diffusivities exhibit only minor variations for all measurement windows (Fig. 11). Notably, the largest discrepancy appears at lower pressures but largely disappears at higher pressures, as evidenced by the ratio of diffusivities calculated using liquid-phase versus confined-phase densities, which is the opposite trend from that observed in adsorption amounts. The same confined-density correction can be embedded in standard CBM reserve audits, replacing the liquid-density assumption.

These findings underscore again the need for refining density correction methods in sorptive gas adsorption studies and propose a new SANS model and methodologies to obtain the adsorbed methane density when confined in the coal matrix. The results indicate that relying on a constant adsorbed density, such as that of liquid methane, overlooks its pressure dependence. Additionally, it fails to account for methane's distinct supercritical behavior under micropore confinement, where the existence of a liquid phase is not guaranteed. Notably, while the choice of density significantly impacts the calculated adsorption capacity, its influence on diffusivity is comparatively minor—underscoring that corrections for adsorbed density are crucial for accurately quantifying gas storage but may be less pivotal for transport properties. In contrast, using the adsorbed methane density derived from SANS could improve the conversion of GSE into absolute adsorption amounts, mitigating underestimation and enhancing predictive models for energy recovery, carbon sequestration, and coal outburst risk assessment. Nonetheless, further studies examining a comprehensive pressure-dependent methane density relationship across diverse coal and carbon materials are needed to equip researchers and industry with a framework for accurate gas storage evaluations.

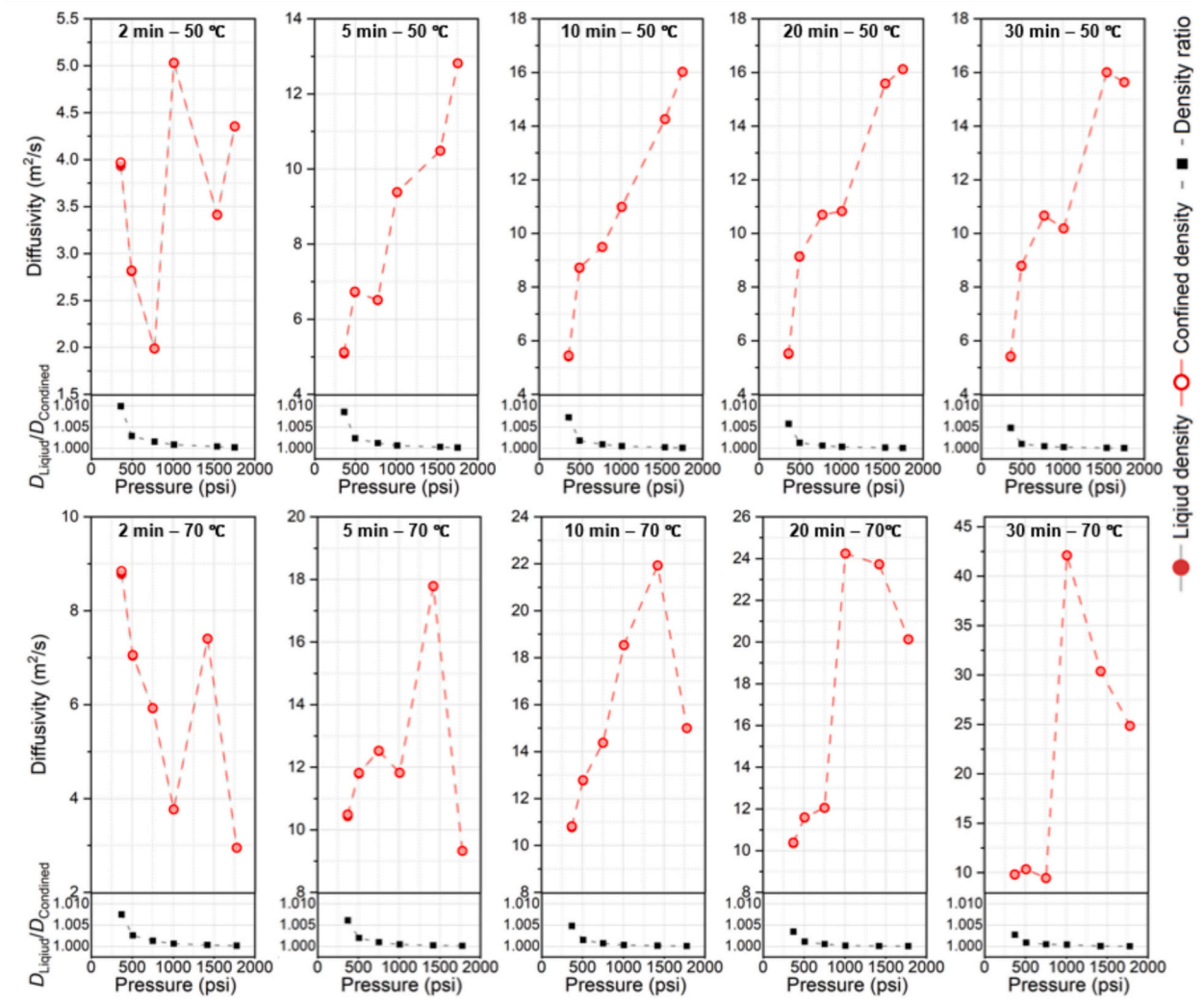

Fig. 11. Diffusivity estimation using two methane density in micropores.

5. Conclusion

This study explores methane storage and adsorption-induced structural alterations in coal using SANS. A new approach for evaluating micropore accessibility is introduced, utilizing SANS data to determine overall accessibility across different pressures and temperatures. A novel fitting model was developed to integrate mechanical constraints within micropores, capturing the impact of pressure-induced adsorbed methane density evolution and its effect in adsorption. By obtaining changes in the scattering length density of the micropores, we show that the adsorbed methane density is notably lower than the conventional liquid-phase assumption. The results are summarized as:

1. Temperature variations induce non-monotonic structural changes in coal, including submicron pore expansion (20–50 °C) and matrix softening near the glass transition temperature (90 °C). SANS revealed lamellar-like aromatic cluster spacing (~14 Å) and pressure-driven compaction, emphasizing coal's elastic response to external gas loading.
2. Micropores exhibit methane densities up to 0.305 g/mL, surpassing bulk-phase predictions due to adsorption potential and capillary condensation effects. The density-pressure relationship follows a power-law trend for sample investigated, with significant pressure amplification ($Rp = 26.9$ at 90 °C) in micropores, underscoring their role as high-energy storage reservoirs.
3. A novel SANS-based accessibility model demonstrates increasing overall micropore utilization with pressure, approaching saturation at ~1600 psi. Closed pores and non-accessible open pores dominate under pressure, while external pressure enhances accessibility, aligning with volumetric adsorption measurements.
4. Adsorption induces microstructural deformation, evidenced by lamellar contraction in the aromatic domains and compaction of the nanoporous matrix. The mechanical constraint model confirms that adsorption can significantly reconfigure micropore geometry while the external pressure simultaneously amplifies the local gas density. However, this effect diminishes at higher pressures as micropore accessibility approaches saturation.
5. SANS delivers the confined methane density, correcting the Langmuir-isotherm underestimation of absolute adsorption while leaving diffusivity largely unaffected; applying this density could sharpen potential adsorption–compression coupling models under nanoscale confinement and, in turn, improves predictions for CBM recovery, CO2 sequestration, and coal-outburst risk.

Nomenclature

Q	Scattering vector, $Å^{-1}$
$I(Q)$	Scattering intensity at scattering vector Q, cm^{-1}
C_{Porod}	Porod constant, cm^{-1} $Å^4$
$I_{incoherent}$	Incoherent scattering intensity, independent of Q, cm^{-1}
Γ_1	1D Correlation Function, normalized between 0 and 1
Γ_3	3D Correlation Function, normalized between 0 and 1
Q^*	Scattering Invariant, cm^{-1} $Å^{-3}$
X	Real-space spacing, Å
ρ^*	Scattering Length Density, 10^{10} cm^{-2}
$\Delta\rho^*$	SLD differences, 10^{10} cm^{-2}
ϕ	Volume fraction of pores
ρ	Mass density, g/mL
C_p	Contrast factor reflecting scattering contrast between pores and rock in larger pore
α	The power-law exponent reflecting fractal nature of the pore wall

CRediT authorship contribution statement

Xinxin He: Writing – original draft, Visualization, Software, Methodology, Investigation, Formal analysis. **Rui Zhang:** Writing – review & editing, Validation, Supervision, Resources, Methodology, Investigation, Data curation, Conceptualization. **Derek Elsworth:** Writing – review & editing, Validation, Supervision, Conceptualization, Investigation, Resources. **Lilin He:** Writing – review & editing, Resources, Data curation, Investigation, Methodology. **Shimin Liu:** Writing – review & editing, Validation, Supervision, Project administration, Methodology, Funding acquisition, Conceptualization, Resources.

Declaration of competing interest

The authors declare that they have no known competing financial interests or personal relationships that could have appeared to influence the work reported in this paper.

Acknowledgments

This research did not receive any specific grant from funding agencies in the public, commercial, or not-for-profit sectors. This research used resources at the High Flux Isotope Reactor, a DOE Office of Science User Facility operated by the Oak Ridge National Laboratory. The beam time was allocated to CG2 on proposal number IPTS-18097.1. This research was financially supported by the National Institute for Occupational Safety and Health (NIOSH) under Grant No. NIOSH-200-2016-90385. This research used resources at the High Flux Isotope Reactor, a DOE Office of Science User Facility operated by the Oak Ridge National Laboratory. The beam time was allocated to CG2 on proposal number IPTS-18097.1.

Appendix A. Supplementary data

Supplementary data to this article can be found online at https://doi.org/10.1016/j.cej.2025.164725.

Data availability

Data will be made available on request.

References

[1] T.A. Moore, Coalbed methane: a review, Int. J. Coal Geol. 101 (2012) 36–81, https://doi.org/10.1016/j.coal.2012.05.011.
[2] I. Gray, Reservoir engineering in coal seams: part 1—the physical process of gas storage and movement in coal seams, SPE Reserv. Eng. 2 (1987) 28–34, https://doi.org/10.2118/12514-PA.
[3] Y. Meng, D. Tang, H. Xu, Y. Qu, Y. Li, W. Zhang, Division of coalbed methane desorption stages and its significance, Pet. Explor. Dev. 41 (2014) 671–677, https://doi.org/10.1016/S1876-3804(14)60080-X.
[4] B. Hu, Y. Cheng, X. He, Z. Wang, Z. Jiang, C. Wang, W. Li, L. Wang, New insights into the CH4 adsorption capacity of coal based on microscopic pore properties, Fuel 262 (2020) 116675, https://doi.org/10.1016/j.fuel.2019.116675.
[5] B. Hu, Y. Cheng, Z. Pan, Classification methods of pore structures in coal: a review and new insight, Gas Science and Engineering 110 (2023) 204876, https://doi.org/10.1016/j.jgsce.2023.204876.
[6] M. Pillalamarry, S. Harpalani, S. Liu, Gas diffusion behavior of coal and its impact on production from coalbed methane reservoirs, Int. J. Coal Geol. 86 (2011) 342–348, https://doi.org/10.1016/j.coal.2011.03.007.
[7] A. Mitra, S. Harpalani, S. Liu, Laboratory measurement and modeling of coal permeability with continued methane production: part 1 – laboratory results, Fuel 94 (2012) 110–116, https://doi.org/10.1016/j.fuel.2011.10.052.
[8] S. Liu, S. Harpalani, M. Pillalamarry, Laboratory measurement and modeling of coal permeability with continued methane production: part 2 – modeling results, Fuel 94 (2012) 117–124, https://doi.org/10.1016/j.fuel.2011.10.053.
[9] S. Liu, S. Harpalani, Permeability prediction of coalbed methane reservoirs during primary depletion, Int. J. Coal Geol. 113 (2013) 1–10, https://doi.org/10.1016/j.coal.2013.03.010.

[10] W. Zhao, Y. Cheng, Z. Pan, K. Wang, S. Liu, Gas diffusion in coal particles: a review of mathematical models and their applications, Fuel 252 (2019) 77–100, https://doi.org/10.1016/j.fuel.2019.04.065.
[11] X. He, P. Yu, A. Eijsink, C. Marone, P. Shokouhi, J. Rivière, S. Liu, D. Elsworth, Co-evolution of specific stiffness and permeability of rock fractures offset in shear, JGR Solid Earth 130 (2025), https://doi.org/10.1029/2024jb030633.
[12] S. Liu, S. Harpalani, A new theoretical approach to model sorption-induced coal shrinkage or swelling, Bulletin 97 (2013) 1033–1049, https://doi.org/10.1306/12181212061.
[13] K. Aminian, Gas transportation in CBM reservoir, in: Coal Bed Methane, Elsevier, 2020, pp. 133–145, https://doi.org/10.1016/B978-0-12-815997-2.00005-6.
[14] J. Zhang, Y. Cheng, X. Cheng, M. Cheng, H. An, J. Yin, K. Zhu, Effect of adsorbed phase density on excess adsorption in coal: an experimental study based on high-pressure adsorption, Energy Fuel 38 (2024) 15270–15283, https://doi.org/10.1021/acs.energyfuels.4c01681.
[15] R.J. Grant, M. Manes, Correlation of some gas adsorption data extending to low pressures and supercritical temperatures, Ind. Eng. Chem. Fund. 3 (1964) 221–224, https://doi.org/10.1021/i160011a009.
[16] X. He, Y. Cheng, B. Hu, Z. Wang, C. Wang, M. Yi, L. Wang, Effects of coal pore structure on methane-coal sorption hysteresis: An experimental investigation based on fractal analysis and hysteresis evaluation, Fuel 269 (2020) 117438, https://doi.org/10.1016/j.fuel.2020.117438.
[17] Hu Biao, Yuanping Cheng, Liang Wang, Kaizhong Zhang, Xinxin He, Minhao Yi, Experimental study on influence of adsorption equilibrium time on methane adsorption isotherm and Langmuir parameter, Adv. Powder Technol. 32 (2021) 4110–4119, https://doi.org/10.1016/j.apt.2021.09.015.
[18] F. Rouquerol, J. Rouquerol, K.S.W. Sing, Adsorption by powders and porous solids: principles, methodology, and applications, Academic Press, San Diego, 1999.
[19] S. Lowell, J.E. Shields, M.A. Thomas, M. Thommes, Characterization of porous solids and powders: surface area, pore size and density, Springer Netherlands, Dordrecht, 2004, https://doi.org/10.1007/978-1-4020-2303-3.
[20] L.E. Arri, D. Yee, W.O. Morgan, M.W. Jeansonne, Modeling coalbed methane production with binary gas sorption, 1992.
[21] M.M. Dubinin, The potential theory of adsorption of gases and vapors for adsorbents with energetically nonuniform surfaces, Chem. Rev. 60 (1960) 235–241, https://doi.org/10.1021/cr60204a006.
[22] Y. Liu, H.A. Li, Y. Tian, Z. Jin, H. Deng, Determination of the absolute adsorption/desorption isotherms of CH4 and n-C4H10 on shale from a nano-scale perspective, Fuel 218 (2018) 67–77, https://doi.org/10.1016/j.fuel.2018.01.012.
[23] L. Wang, Z. Chen, C. Wang, D. Elsworth, W. Liu, Reassessment of coal permeability evolution using steady-state flow methods: the role of flow regime transition, Int. J. Coal Geol. 211 (2019) 103210, https://doi.org/10.1016/j.coal.2019.103210.
[24] H. Li, S. Shi, J. Lu, Q. Ye, Y. Lu, X. Zhu, Pore structure and multifractal analysis of coal subjected to microwave heating, Powder Technol. 346 (2019) 97–108, https://doi.org/10.1016/j.powtec.2019.02.009.
[25] Y. Tian, C. Yan, Z. Jin, Characterization of methane excess and absolute adsorption in various clay nanopores from molecular simulation, Sci. Rep. 7 (2017) 12040, https://doi.org/10.1038/s41598-017-12123-x.
[26] J. Xiong, X. Liu, L. Liang, X. Wei, P. Xu, Investigation of the factors influencing methane adsorption on illite, Energy Sci. Eng. 7 (2019) 3317–3331, https://doi.org/10.1002/ese3.501.
[27] K.M. Nikolaev, M.M. Dubinin, Concerning adsorptional properties of carbon adsorbents 3, A study of adsorption isotherms of gases and vapors on active carbons over a wide interval of temperatures, including the critical region, Russ Chem Bull 7 (1958) 1124–1133, https://doi.org/10.1007/BF00914939.
[28] J.J. Haydel, R. Kobayashi, Adsorption equilibria in methane-propane-silica gel system at high pressures, Ind. Eng. Chem. Fund. 6 (1967) 546–554, https://doi.org/10.1021/i160024a010.
[29] M. Gasparik, A. Ghanizadeh, P. Bertier, Y. Gensterblum, S. Bouw, B.M. Krooss, High-pressure methane sorption isotherms of black shales from the Netherlands, Energy Fuel 26 (2012) 4995–5004, https://doi.org/10.1021/ef300405g.
[30] Y. Gensterblum, A. Merkel, A. Busch, B.M. Krooss, High-pressure CH4 and CO2 sorption isotherms as a function of coal maturity and the influence of moisture, Int. J. Coal Geol. 118 (2013) 45–57, https://doi.org/10.1016/j.coal.2013.07.024.
[31] Y. Gensterblum, A. Busch, B.M. Krooss, Molecular concept and experimental evidence of competitive adsorption of H2O, CO2 and CH4 on organic material, Fuel 115 (2014) 581–588, https://doi.org/10.1016/j.fuel.2013.07.014.
[32] X. Cheng, Y. Cheng, C. Wang, B. Hu, J. Wang, Calculation methods on methane adsorption phase density in coal: a critical review and new insights, Chem. Eng. J. 472 (2023) 144778, https://doi.org/10.1016/j.cej.2023.144778.
[33] Y. Yao, D. Liu, S. Xie, Quantitative characterization of methane adsorption on coal using a low-field NMR relaxation method, Int. J. Coal Geol. 131 (2014) 32–40, https://doi.org/10.1016/j.coal.2014.06.001.
[34] D. Liu, Y. Yao, Y. Chang, Measurement of adsorption phase densities with respect to different pressure: potential application for determination of free and adsorbed methane in coalbed methane reservoir, Chem. Eng. J. 446 (2022) 137103, https://doi.org/10.1016/j.cej.2022.137103.
[35] X. Cheng, Y. Cheng, C. Wang, J. Wang, B. Hu, Methane as probes for characterizing pore volume in coalbed gas reservoir: Expanding the pore analysis method, Fuel 389 (2025) 134563, https://doi.org/10.1016/j.fuel.2025.134563.
[36] L. Ortiz, B. Kuchta, L. Firlej, M.W. Roth, C. Wexler, Methane adsorption in nanoporous carbon: the numerical estimation of optimal storage conditions, Mater. Res. Express 3 (2016) 055011, https://doi.org/10.1088/2053-1591/3/5/055011.
[37] S. Wu, L. Wang, C. Liu, S. Su, Z. Lu, X. He, Q. Yang, L. Guo, Experimental study of deformation induced by high-pressure methane adsorption and desorption: Insights into anisotropy and hysteresis characteristics, Int. J. Rock Mech. Min. Sci. 186 (2025) 106035, https://doi.org/10.1016/j.ijrmms.2025.106035.
[38] A.P. Radlinski, Small-angle neutron scattering and the microstructure of rocks, Rev. Mineral. Geochem. 63 (2006) 363–397, https://doi.org/10.2138/rmg.2006.63.14.
[39] I. Grillo, Small-angle neutron scattering and applications in soft condensed matter, in: R. Borsali, R. Pecora (Eds.), Soft matter characterization, Springer Netherlands, Dordrecht, 2008, pp. 723–782, https://doi.org/10.1007/978-1-4020-4465-6_13.
[40] T. Brückel, Forschungszentrum Jülich (Eds.), Neutron Scattering: Lectures of the JCNS Laboratory Course Held at Forschungszentrum Jülich and the Research Reactor FRM II of TU Munich in Cooperation with RWTH, Aachen and University of Münster, Forschungszentrum Jülich, Jülich, 2012.
[41] J. Bahadur, Y.B. Melnichenko, M. Mastalerz, A. Furmann, C.R. Clarkson, Hierarchical pore morphology of cretaceous shale: a small-angle neutron scattering and Ultrasmall-angle neutron scattering study, Energy Fuel 28 (2014) 6336–6344, https://doi.org/10.1021/ef501832k.
[42] R. Zhang, S. Liu, L. He, T.P. Blach, Y. Wang, Characterizing anisotropic pore structure and its impact on gas storage and transport in coalbed methane and shale gas reservoirs, Energy Fuel 34 (2020) 3161–3172, https://doi.org/10.1021/acs.energyfuels.0c00109.
[43] R. Zhang, S. Liu, J. Bahadur, D. Elsworth, Y. Wang, G. Hu, Y. Liang, Changes in pore structure of coal caused by coal-to-gas bioconversion, Sci. Rep. 7 (2017) 3840, https://doi.org/10.1038/s41598-017-04110-z.
[44] S. Liu, R. Zhang, Anisotropic pore structure of shale and gas injection-induced nanopore alteration: a small-angle neutron scattering study, Int. J. Coal Geol. 219 (2020) 103384, https://doi.org/10.1016/j.coal.2020.103384.
[45] J. Bahadur, L.F. Ruppert, V. Pipich, R. Sakurovs, Y.B. Melnichenko, Porosity of the Marcellus shale: a contrast matching small-angle neutron scattering study, Int. J. Coal Geol. 188 (2018) 156–164, https://doi.org/10.1016/j.coal.2018.02.002.
[46] R. Zhang, S. Liu, A. San-Miguel, R. Schweins, S. Le Floch, V. Pischedda, Nanoscale coal deformation and alteration of porosity and pore orientation under uniaxial compression: An in situ SANS study, Rock Mech. Rock. Eng. 54 (2021) 3593–3608, https://doi.org/10.1007/s00603-020-02321-x.
[47] R. Zhang, X. Wang, S. Liu, L. He, C. Song, X. Jiang, T.P. Blach, Discovering inherent characteristics of polyethylenimine-functionalized porous materials for CO_2 capture, ACS Appl. Mater. Interfaces. 11 (40) (2019) 36515–36524, https://doi.org/10.1021/acsami.9b08496.
[48] A.P. Radlinski, T. Blach, Multiscale micro-architecture of pore space in rocks: size, shape, deformation and accessibility determined by small-angle neutron scattering (SANS), Eur. Phys. J. E 46 (2023) 78, https://doi.org/10.1140/epje/s10189-023-00336-0.
[49] R. Zhang, S. Liu, J. Bahadur, D. Elsworth, Y. Melnichenko, L. He, Y. Wang, Estimation and modeling of coal pore accessibility using small angle neutron scattering, Fuel 161 (2015) 323–332, https://doi.org/10.1016/j.fuel.2015.08.067.
[50] A.P.R. Eberle, H.E. King, P.I. Ravikovitch, C.C. Walters, G. Rother, D. J. Wesolowski, Direct measure of the dense methane phase in gas shale organic porosity by neutron scattering, Energy Fuel 30 (2016) 9022–9027, https://doi.org/10.1021/acs.energyfuels.6b01548.
[51] Y.B. Melnichenko, G.D. Wignall, D.R. Cole, H. Frielinghaus, Density fluctuations near the liquid-gas critical point of a confined fluid, Phys. Rev. E 69 (2004) 057102, https://doi.org/10.1103/PhysRevE.69.057102.
[52] Y.B. Melnichenko, G.D. Wignall, D.R. Cole, H. Frielinghaus, Adsorption of supercritical CO2 in aerogels as studied by small-angle neutron scattering and neutron transmission techniques, J. Chem. Phys. 124 (2006) 204711, https://doi.org/10.1063/1.2202324.
[53] N.C. Gallego, L. He, D. Saha, C.I. Contescu, Y.B. Melnichenko, Hydrogen confinement in carbon nanopores: extreme densification at ambient temperature, J. Am. Chem. Soc. 133 (2011) 13794–13797, https://doi.org/10.1021/ja202432x.
[54] L. He, Y.B. Melnichenko, N.C. Gallego, C.I. Contescu, J. Guo, J. Bahadur, Investigation of morphology and hydrogen adsorption capacity of disordered carbons, Carbon 80 (2014) 82–90, https://doi.org/10.1016/j.carbon.2014.08.041.
[55] J. Bahadur, Y.B. Melnichenko, L. He, C.I. Contescu, N.C. Gallego, J.R. Carmichael, SANS investigations of CO2 adsorption in microporous carbon, Carbon 95 (2015) 535–544, https://doi.org/10.1016/j.carbon.2015.08.010.
[56] R. Zhang, S. Liu, Investigating hierarchical gas confinement in high-rank coal through small-angle neutron scattering, Energy Fuel 35 (2021) 13109–13123, https://doi.org/10.1021/acs.energyfuels.1c01693.
[57] R. Zhang, S. Liu, L. Fan, T.P. Blach, G. Sang, Unraveling high-pressure gas storage mechanisms in shale nanopores through SANS, Environ. Sci. Nano 8 (2021) 2706–2717, https://doi.org/10.1039/D1EN00419K.
[58] J.S. Gethner, The determination of the void structure of microporous coals by small-angle neutron scattering: void geometry and structure in Illinois no. 6 bituminous coal, J. Appl. Phys. 59 (1986) 1068–1085, https://doi.org/10.1063/1.336543.
[59] L. He, Y.B. Melnichenko, M. Mastalerz, R. Sakurovs, A.P. Radlinski, T. Blach, Pore accessibility by methane and carbon dioxide in coal as determined by neutron scattering, Energy Fuel 26 (2012) 1975–1983, https://doi.org/10.1021/ef201704t.
[60] A. Gooden, Mineralogy database, Ref. Rev. (2004), https://doi.org/10.1108/09504120410543200.
[61] G.R. Dyrkacz, C.A.A. Bloomquist, L. Ruscic, High-resolution density variations of coal macerals, Fuel 63 (1984) 1367–1373, https://doi.org/10.1016/0016-2361(84)90339-9.
[62] W.T. Heller, M. Cuneo, L. Debeer-Schmitt, C. Do, L. He, L. Heroux, K. Littrell, S. V. Pingali, S. Qian, C. Stanley, V.S. Urban, B. Wu, W. Bras, The suite of small-angle

neutron scattering instruments at oak Ridge National Laboratory, J. Appl. Cryst. 51 (2018) 242–248, https://doi.org/10.1107/S1600576718001231.
[63] W.T. Heller, J. Hetrick, J. Bilheux, J.M.B. Calvo, W.-R. Chen, L. DeBeer-Schmitt, C. Do, M. Doucet, M.R. Fitzsimmons, W.F. Godoy, G.E. Granroth, S. Hahn, L. He, F. Islam, J. Lin, K.C. Littrell, M. McDonnell, J. McGaha, P.F. Peterson, S.V. Pingali, S. Qian, A.T. Savici, Y. Shang, C.B. Stanley, V.S. Urban, R.E. Whitfield, C. Zhang, W. Zhou, J.J. Billings, M.J. Cuneo, R.M.F. Leal, T. Wang, B. Wu, Drtsans: the data reduction toolkit for small-angle neutron scattering at oak Ridge National Laboratory, SoftwareX 19 (2022) 101101, https://doi.org/10.1016/j.softx.2022.101101.
[64] R. Zhang, S. Liu, Y. Wang, Fractal evolution under in situ pressure and sorption conditions for coal and shale, Sci. Rep. 7 (2017) 8971, https://doi.org/10.1038/s41598-017-09324-9.
[65] S. Liu, R. Zhang, Z. Karpyn, H. Yoon, T. Dewers, Investigation of accessible pore structure evolution under pressurization and adsorption for coal and shale using small-angle neutron scattering, Energy Fuel 33 (2019) 837–847, https://doi.org/10.1021/acs.energyfuels.8b03672.
[66] J. Yu, J.A. Lucas, T.F. Wall, Formation of the structure of chars during devolatilization of pulverized coal and its thermoproperties: a review, Prog. Energy Combust. Sci. 33 (2007) 135–170, https://doi.org/10.1016/j.pecs.2006.07.003.
[67] H. Kobayashi, J.B. Howard, A.F. Sarofim, Coal devolatilization at high temperatures, Symp. Combust. 16 (1977) 411–425, https://doi.org/10.1016/S0082-0784(77)80341-X.
[68] L.M. Lucht, J.M. Larson, N.A. Peppas, Macromolecular structure of coals. 9. Molecular structure and glass transition temperature, Energy Fuel 1 (1987) 56–58, https://doi.org/10.1021/ef00001a010.
[69] E.J. LeBoeuf, W.J. Weber, Macromolecular characteristics of natural organic matter. 1. Insights from glass transition and Enthalpic relaxation behavior, Environ. Sci. Technol. 34 (2000) 3623–3631, https://doi.org/10.1021/es991103o.
[70] C.R. Ward, Analysis, origin and significance of mineral matter in coal: An updated review, Int. J. Coal Geol. 165 (2016) 1–27, https://doi.org/10.1016/j.coal.2016.07.014.
[71] S. Wu, G. Gong, K. Yan, Y. Sun, L. Zhang, Polycyclic aromatic hydrocarbons in edible oils and fatty foods: occurrence, formation, analysis, change and control, in: Advances in food and nutrition research, Elsevier, 2020, pp. 59–112, https://doi.org/10.1016/bs.afnr.2020.02.001.
[72] Z. Feng, T. Cai, D. Zhou, D. Zhao, Y. Zhao, C. Wang, Temperature and deformation changes in anthracite coal after methane adsorption, Fuel 192 (2017) 27–34, https://doi.org/10.1016/j.fuel.2016.12.005.
[73] K. Yang, X. Lu, Y. Lin, A.V. Neimark, Deformation of coal induced by methane adsorption at geological conditions, Energy Fuel 24 (2010) 5955–5964, https://doi.org/10.1021/ef100769x.
[74] F. Kleitz, F. Bérubé, R. Guillet-Nicolas, C.-M. Yang, M. Thommes, Probing adsorption, pore condensation, and hysteresis behavior of pure fluids in three-dimensional cubic mesoporous KIT-6 silica, J. Phys. Chem. C 114 (2010) 9344–9355, https://doi.org/10.1021/jp909836v.
[75] P.J. Linstrom, W.G. Mallard, The NIST chemistry WebBook: a chemical data resource on the internet, J. Chem. Eng. Data 46 (2001) 1059–1063, https://doi.org/10.1021/je000236i.
[76] X. Cheng, Y. Cheng, B. Hu, X. He, Quantitative analysis of difference in CH 4 and CO 2 adsorption capacity in coal based on adsorption model, J. Nat. Gas Sci. Eng. 102 (2022) 104541, https://doi.org/10.1016/j.jngse.2022.104541.
[77] X. He, D. Elsworth, S. Liu, Millisecond-resolved gas sorption kinetics and time-dependent diffusivity of coal, Rock Mech. Rock Eng. (2024), https://doi.org/10.1007/s00603-024-03952-0.